

GPPS-TC-2022-0096

Simulation of a Multistage Compressor at Low Load Operation with Additional Bleed Air Extraction for Minimum Environmental Load Reduction

Georgios Goinis

German Aerospace Center (DLR)

Georgios.Goinis@dlr.de

Cologne, Germany

Marcello Benvenuto

Ansaldo Energia

Marcello.Benvenuto@ansaldoenergia.com

Genoa, Italy

Stefano Gino Mosele

Ansaldo Energia

StefanoGino.Mosele@ansaldoenergia.com

Genoa, Italy

Andrea Schneider

Ansaldo Energia

Andrea.Schneider@ansaldoenergia.com

Genoa, Italy

ABSTRACT

The need for more flexible operation of gas-fired power plants has led manufacturers to exploit possibilities to retrofit existing systems and increase turndown capabilities, lowering the minimum environmental load (MEL) - the lowest output at which the unit can operate and still meet environmental emissions limits. A possible measure for the compressor to enable a reduced MEL is to extract significant mass flow rates through the bleed ports in operation with a closed IGV to lower the mass flow entering the combustor, enabling a further load reduction while maintaining emissions. For this measure to be implemented, a stable operation of the compressor has to be ensured at the reduced MEL conditions. It is well known that bleed-air offtake at full speed shifts the loading towards the rear stages of the compressor. At MEL, the rear stages already operate at an increased loading compared to base-load. Therefore, to confirm the viability of bleed offtake as a turndown strategy, the effects on performance and stability have to be quantified for operation at MEL. Of particular interest is how an increase in air extraction through the bleed ports influences the stability of the compressor at MEL, especially when the offtake is from low pressure. Information on the degradation of the stability margin due to the additional bleed-air extraction at MEL is gained through numerical simulations. Full-compressor CFD simulations of an F-class gas turbine at reduced MEL conditions are performed. The influence of several geometrical and numerical modeling details is studied, and the model is validated against a comprehensive set of experimental data. The numerical results show good agreement with the experimental data, even with increased bleed air extraction. It can be concluded that bleed-air extraction is a capable method of reducing the compressor discharge mass flow rate significantly. The extraction rate is limited by the stability of the last compressor stages. Further analysis should be performed to verify the integrity of the whole GT at operation under such conditions, e.g., the thermal state of hot parts.

INTRODUCTION

The rise of renewable energy is rapidly changing the energy landscape. Low variable operating costs for renewables, such as wind and solar, lead to fossil-fueled power generation being curtailed in favor of renewable loads (Lorenczik et al., 2020). This periodic adjustment of the power output generated by fossil-fueled power plants, the so-called cycling, is required to take place with increased flexibility, as the share of renewables in the market is rising.

With the need for higher flexibility, capacity that was designed for base-load operation is required to provide load-following or even peaking service without penalties on life, cost and emission. Especially combined cycle gas turbines (CCGTs) are suitable for this purpose, as they can respond to changes in load faster than conventional steam power plants. Therefore, gas-fired capacity is increasingly being shifted from base load to part/minimum load with the main target to provide backup capacity and enable higher renewable shares. However, turndown limitations and increased mechanical

and thermal stress put some constraints on the cycling of CCGTs. In this context, the low part-load operation offers an alternative to a start-stop cycle, avoiding start-stop cycle stress and cost, as well as start-up emissions.

A key issue at low part-load operation is to keep the emissions of mono-nitrogen oxides (NO_x) and especially carbon monoxides (CO) under control. A significant increase in CO emissions, occurring at part load in gas turbines, is attributed to a reduced combustion temperature and incomplete combustion of the natural gas (Hung, 1993). While at base-load, high firing temperatures lead to most of the CO being oxidized to carbon dioxide (CO₂), in the lower load range, the firing temperature drops below a value where the combustion is complete. The oxidation of CO is quenched by cool regions near the walls of the combustor, resulting in less conversion of CO to CO₂ and hence, increased CO emissions. The temperature limit for a complete burnout depends on the burner design and the operation concept of the engine (i.e., the fuel-to-air ratio) (Magni et al., 2016). The lower combustion temperatures and fuel volumes burned at reduced load result in lower or equal absolute NO_x and CO₂ emissions. However, since the reduction in power and efficiency is stronger than the reduction in absolute emissions, the NO_x and CO₂ specific emission factors at reduced load are also higher than at full load (Gonzalez-Salazar et al., 2018).

A constraint for low load operation is the minimum environmental load (MEL), also called minimum (emissions-) compliant load (MCL). It is the lowest power output at which the gas turbine can operate without violating emission limits for NO_x and CO. A further load reduction would result in possible emission exceedances. Heavy-duty gas turbines (that have not been upgraded) offer current MEL values of around 40–50% of full load (Gonzalez-Salazar et al., 2018). In CCGTs, the turbine outlet temperature must be kept high enough to produce sufficient steam for the steam turbine. Therefore the MEL of CCGTs is usually at about 50% of full load. It is expected that these values will reduce to 20% in a simple cycle and 30% in a combined cycle in the future (Gonzalez-Salazar et al., 2018) by implementing new concepts and upgrade packages.

Concepts to lower part-load operation

A low part-load upgrade aims at improving the combustion of the gas turbine by keeping the flame temperature at higher levels. The key to success for improved combustion behavior at part load is mainly the reduction of the burner air mass flow (Magni et al., 2016). Reducing the amount of burner air can be done in different ways:

- IGV extra closure: Reducing the compressor inlet mass flow by (further) closing the IGV.
- Anti-Icing (AI) system: Air Re-circulation from the compressor plenum to the inlet via the AI system.
- Blow-off: Bypassing the combustor by injecting extra bleed air from the compressor plenum or the compressor bleeds to the turbine or exhaust of the engine.

Some experience has been gathered on the effectiveness of these approaches.

Nag et al. (2010, 2008) describe a low load turndown upgrade for Siemens F- and G-class GTs. The design is based on a combination of reducing the compressor airflow by allowing for more closed IGV settings and bypassing compressed air around the combustor. The extra bleed air is bypassed from the combustor shell and compressor bleeds (stages 10/13 and 11 for F- and G-class, respectively) into the turbine stages and the exhaust. This, along with a combination of IGV and secondary air system controls, allows a maximum turndown of approximately 40% GT load while maintaining CO emissions out of the engine below the limit and even 28% GT load while maintaining CO emissions out of the exhaust stack below the limit using a CO catalyst. Nag et al. (2010) suggest that there are potential methods to further improve the turndown capability at lower ambient temperatures by implementing an inlet heating upgrade.

Magni et al. (2016) describe the development and testing of an upgrade package for the GE GT13E2 for improved MEL, which allows the GT to operate down to 26% relative load. They state that only a combination of several measures improves the MEL of the gas turbine and the combined cycle efficiency. Three measures have been combined: Extra VIGV closing, air recirculation using the anti-icing system, and a redistribution of the fuel gas to fewer burners together with a partial burner switch off (Therkorn et al., 2015). Magni et al. (2016) also investigated a compressor bypass solution but found that the recirculation (via the AI-system) showed a higher potential to maximize the efficiency of the part-load operation and minimize the concept integration effort, as the plant chosen for the experiments already had an AI system.

Cioffi et al. (2014) describe a strategy to reduce the MEL of heavy-duty axial gas turbines using the compressor air bleeding lines (blow-off lines). Field tests showed the capability to decrease the MEL significantly. Further techniques they tested to lower the MEL are combustion and secondary air system (SAS) improvements (Malavasi et al., 2013) and the use of the AI-line. They found a limited effect of SAS settings on GT power turndown. A higher effect could be achieved with AI insertion. The best performances were achieved with a blow-off (BO) opening.

Aim of the study

In a previous study (Mosele et al., 2019; Hedkvist, 2019) the optimal distribution of mass-flow extraction through the three available blow-off lines was examined employing compressor through-flow simulations. The results show that the last stator row limits the overall stability of the compressor at MEL and hence the maximum possible extraction. In terms of stability and compressor power input, extracting the mass flow at the first bleed is beneficial.

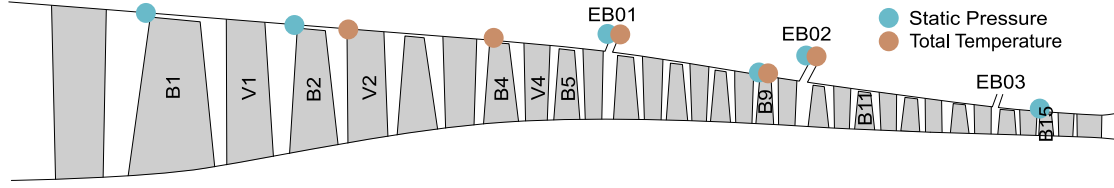


Figure 1 : Sketch of Ansaldo F-Class Gas-Turbine Compressor with location of probes.

| case | ambient condition | IGV/V01 position | EB01 \dot{m} | γ_{GV} [%] | γ_{V1} [%] | \dot{m}_{in} [%] | RH [%] | T_{amb} [%] | p_{amb} [%] | \dot{m}_{EB01} [% of \dot{m}_{in}] | \dot{m}_{EB02} | \dot{m}_{EB03} |
|------|-------------------|------------------|----------------|-------------------|-------------------|--------------------|--------|---------------|---------------|---|------------------|------------------|
| T23 | hot | MEL | MEL | 100 | 100 | 100 | 100 | 100 | 100 | 0.3 | MEL | MEL |
| T21R | dry | MEL | MEL | 99 | 99 | 104 | 33 | 94 | 102 | 0.5 | MEL | MEL |
| T26R | | x | MEL | 108 | 110 | 95 | 117 | 92 | 103 | 0.5 | MEL | MEL |
| T28R | | MEL | x | 101 | 100 | 105 | 96 | 93 | 102 | 6.8 | MEL | MEL |
| T30R | | MEL | x | 102 | 102 | 102 | 119 | 92 | 102 | 10.7 | MEL | MEL |
| T32R | | x | x | 109 | 111 | 91 | 114 | 92 | 102 | 8.9 | MEL | MEL |

Table 1 : Experimental test cases. Relative values normalized with T23.

In the current study, the results of the through-flow studies are further assessed through 3D-CFD studies. An appropriate CFD model is established and validated with experimental data. Then, the influence of high blow-off mass-flow rates on the performance and stability of the compressor is studied in order to assess the feasibility of this measure to enable operation at further reduced load.

TEST CASE, INSTRUMENTATION, EXPERIMENTAL DATA

The study is based on a state-of-the-art F-Class gas turbine by Ansaldo Energia. The compressor consists of 15 stages, IGV and OGV (fig. 1). IGV and the first stator blade have a variable stagger configuration, which allows for an independent stagger angle variation of these two rows. All vanes, excluding VGVs, are shrouded. The compressor is equipped with blow-off pipelines, which extract air from different outer extraction plenums (bleeding chambers), positioned at low (EB01), mid (EB02), and high (EB03) pressure compressor sections at the outer casing (see fig. 1). They are intended to avoid critical conditions during start-up by decreasing the air mass flow rate in the following compressor stages to avoid choking of the rear stages and reducing the back pressure of the front stages. During nominal rotation speed GT operation, the BO valves are usually closed (Cioffi et al., 2014).

For validation purposes, the simulation results are compared with field data obtained during a test campaign carried out by Ansaldo Energia. The boundary conditions for the steady-state full compressor simulations are derived from these measurements. Operation points measured during the campaign are listed in table 1. All measured operating points represent conditions at MEL with variations in ambient conditions, vane positions, and blow-off valve positions. Standard MEL values are marked with “MEL”. The values are normalized with those of T23. An “x” indicates an increased value as compared to standard MEL conditions, i.e., an increased IGV closure or an increased blow-off valve opening.

The measured data of the compressor includes IGV angle, extraction slot valve position, ambient temperature, pressure, relative humidity, grid frequency, compressor inlet and outlet temperature and pressure. To monitor the behavior of the compressor in more detail, additional instrumentation has been applied throughout the compressor at the casing and inside the extraction slots (fig. 1). The instrumentation consists of six static pressure transducers (upstream rotors 1, 2, 9, and 15, and inside the extraction slots EB1 and EB2) and five total temperature taps (upstream stator 2 and 4 and upstream rotor 9, as well as inside the extraction slots EB1 and EB2). The data of T23 has been obtained at a previous campaign with slightly different instrumentation.

COMPUTATIONAL FRAMEWORK

The simulation of multistage axial compressors can be a challenge, in particular when dealing with off-design operating conditions (Cozzi et al., 2017, 2018). This is especially true for simulations at MEL and at reduced MEL with high mass flow extraction through the bleed ports. The main challenges are high separation regions at the blades, especially at the first rows, as well as back-flow regions in the vicinity of the bleed extraction ports, which can lead to difficulties in achieving stable RANS solutions. Therefore, the model has to be carefully evaluated. Different computational meshes, solver settings, and the influence of certain modeling details, such as interface positions and geometric details, are analyzed to obtain a CFD model, that provides stable, accurate solutions.

All simulations are performed using the DLR turbomachinery flow solver TRACE (Becker et al., 2010). It has been

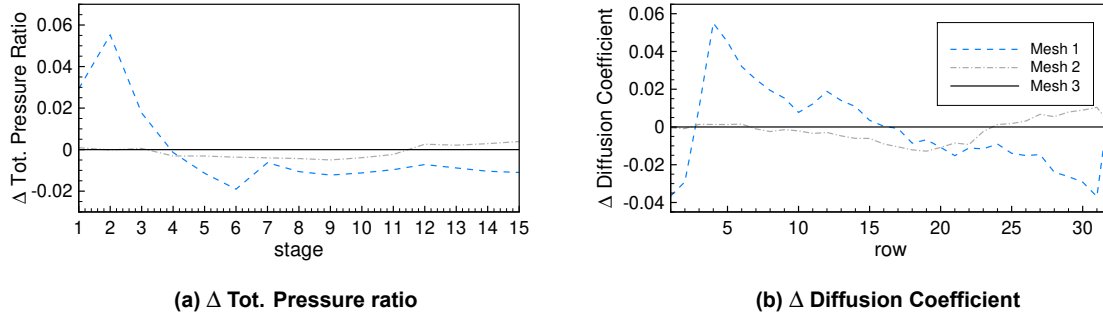


Figure 2 : Mesh comparison at MEL operating point. Delta-plots in relation to mesh 3.

| Mesh | Radial resolution [nodes] | y+ blades [-] | y+ endwalls [-] | Cells total [million] | Cells per row (average) [million] | $\Delta \dot{m}_{in}$ [%] | $\Delta T_{tot.out}$ [%] |
|------|------------------------------|------------------|--------------------|--------------------------|--------------------------------------|------------------------------|-----------------------------|
| 1 | 85 | > 50 | > 50 | 29 | 0.9 | -0.82 | -3.52 |
| 2 | 85 | < 1 | > 50 | 32 | 1 | -0.01 | -2.00 |
| 3 | 129 | < 1 | < 1 | 97 | 3 | -0.04 | -1.55 |

Table 2 : Comparison of meshes. Parameters and results in relation to experimental data for an operating point at MEL.

validated extensively for a large number of turbomachinery test cases (Eulitz, 1999; Hummel, 2002; Schmitt et al., 2001). RANS simulations are performed for the blow-off studies using an SST turbulence model with extensions for stagnation point anomaly, rotational effects, and reattachment. The convective flows are modeled with a TVD upwind scheme (Roe, 1981), combined with the MUSCL extrapolation (van Leer, 1979). For stationary simulations, non-reflecting boundary conditions are used (Giles, 1990). The coupling between blade rows is achieved by mixing planes (Saxer and Giles, 1993; Holmes, 2008). A conservative zonal approach (Yang and Weber, 2002) is used to attach the bleed ports as well as between the last stator and outlet guide vane. The gas is modeled as a composition of air and water vapor to account for humidity. A thermally perfect gas, sometimes also referred to as a semi-perfect gas, is assumed, i.e., a fluid that obeys the thermal equation of state and for which specific internal energy, specific enthalpy, and specific heat are functions of temperature only. An adiabatic flow is assumed. At the entrance of the simulation area, measured radial distributions of total pressure, total temperature, and flow angles are prescribed. At the outlet of the computational domain, the static pressure at mid-span is given, and a radial equilibrium is enforced.

Different fully structured meshes are used for comparison, generated with the DLR Institute of Propulsion Technology's in-house mesh generator "PyMesh". The key parameters are listed in tab. 2. Clearances of the variable vanes are not modeled and hence not accounted for in the simulations. The effect of seal cavity flow on the main stream is not considered.

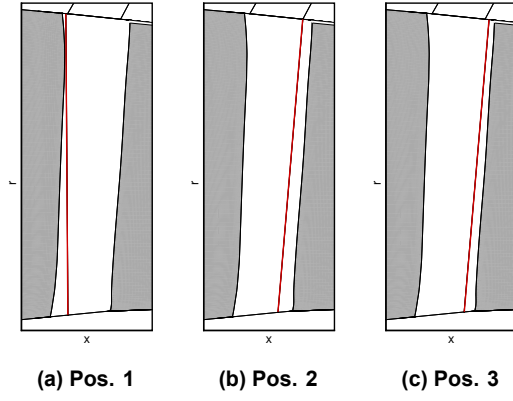
A mesh comparison is performed for the MEL operating point T23 (tab. 1). It can be observed that an approximation of the boundary layer using a wall-function approach and a meshing with $y^+ > 50$ at the blade surfaces does not accurately capture the challenging flow regime with the various separations in the first stages. This leads to false predictions in mass flow, losses, and pressure rise, especially for the first three stages. Consequently, the pressure rise capability of these stages is overestimated, leading to a wrong matching of the machine with the last stages being slightly lower loaded (fig. 2). For the evaluation of row and stage-wise data, analysis planes have been positioned up and downstream of the leading and trailing edges of every row.

At MEL conditions, the loading of the last stages is especially critical. Therefore a mesh resolving the blade boundary layers is needed in order to obtain the correct matching. A comparison between meshes 2 and 3 shows that a significant increase in mesh resolution from 32 to 97 million cells does not change the results significantly. Several comparisons of different operating conditions support this conclusion. Therefore, for the study at hand mesh 2 is used, as it provides an advantage in computational costs. However, selected significant operating points, such as close to stall, are simulated with mesh 3 as well.

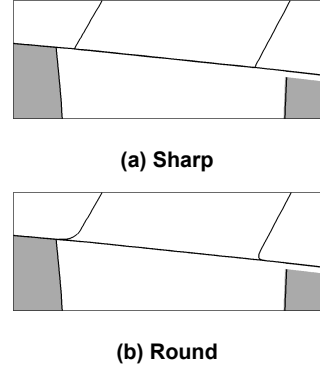
Bleed port modeling

The bleed port geometries are modeled as circumferential extraction slots. At the exit of the extraction ports, the mass flow rate is prescribed. A comparison between different modeling approaches is made, to ensure the bleed ports can handle significant amounts of mass flow rates. A very high extraction rate of 20% of the inlet mass flow through the first external bleed port (EB01) is chosen for the study. This rate exceeds the values which are expected during operation by far.

Studied are different positions of the interface between stator and rotor, as shown in fig. 3, as well as a round vs. a



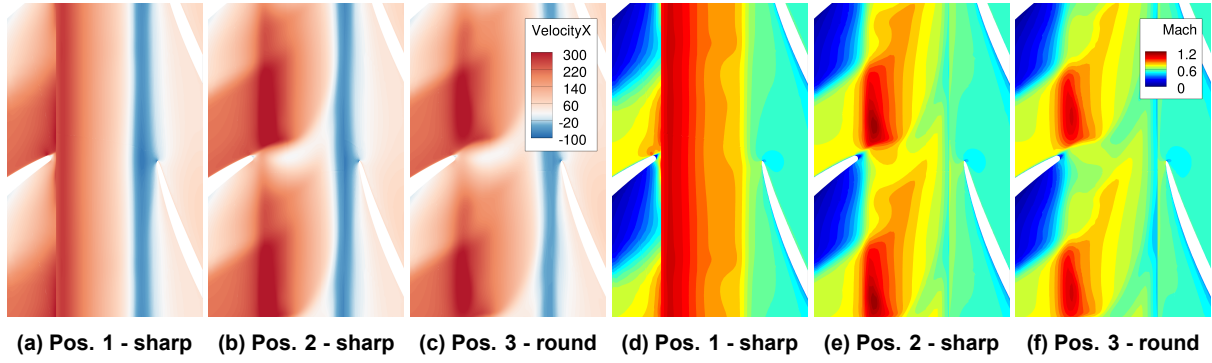
(a) Pos. 1 (b) Pos. 2 (c) Pos. 3



(a) Sharp

(b) Round

Figure 3 : Mixing plane positions at EB01. Figure 4 : Modelling the bleed port corner.



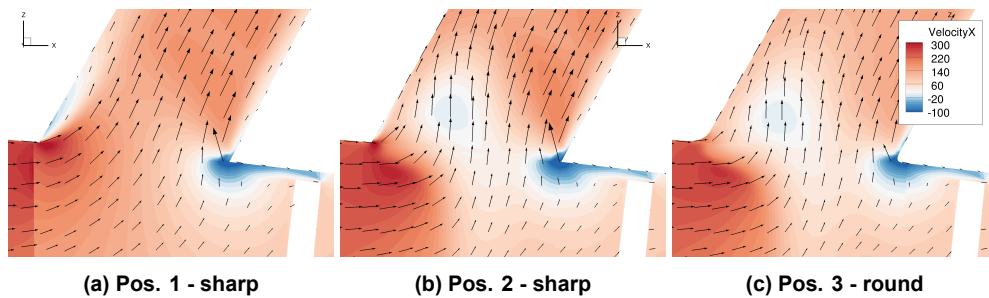
(a) Pos. 1 - sharp (b) Pos. 2 - sharp (c) Pos. 3 - round (d) Pos. 1 - sharp (e) Pos. 2 - sharp (f) Pos. 3 - round

Figure 5 : Contour plot of axial velocity and Mach number on S1 plane at 99% channel height. Comparison of cases 1, 2 & 3: Interface pos. 1 with sharp edges (a,d), pos. 2 with sharp edges (b,e) and pos. 3 with round edges (c,f) at bleed port EB01 with 20% extraction.

sharp edge of the bleed port (fig. 4). With sharp edges at the bleed port, all mixing plane positions are possible, whereas with round edges at the bleed port, only position 3 downstream of the bleed port is possible. Although the real geometry of the bleed port has round edges, a position of the interface plane so close to the leading edge of the rotor (fig. 3c) is not favorable, as it can lead to numerical instabilities. On the other hand, a sharp edge could lead to more distinct separations, blocking the bleed-port channel and limiting the possible extraction rates. For comparison, three cases are looked at in detail:

- Case 1: Mixing plane at position 1. EB01 with sharp edges.
- Case 2: Mixing plane at position 2. EB01 with sharp edges.
- Case 3: Mixing plane at position 3. EB01 with round edges.

Fig. 5 shows a comparison of the three different modeling approaches in terms of S1 planes at 99% channel height at the location at EB01. The plots of axial velocity show a back-flow occurring in the leading edge region of rotor 6 blade tip



(a) Pos. 1 - sharp

(b) Pos. 2 - sharp

(c) Pos. 3 - round

Figure 6 : Contour plots of axial velocity at EB01. Comparison of cases 1, 2 & 3: Interface pos. 1 with sharp edges (a), pos. 2 with sharp edges (b) and pos. 3 with round edges (c) at bleed port EB01 with 20% extraction.

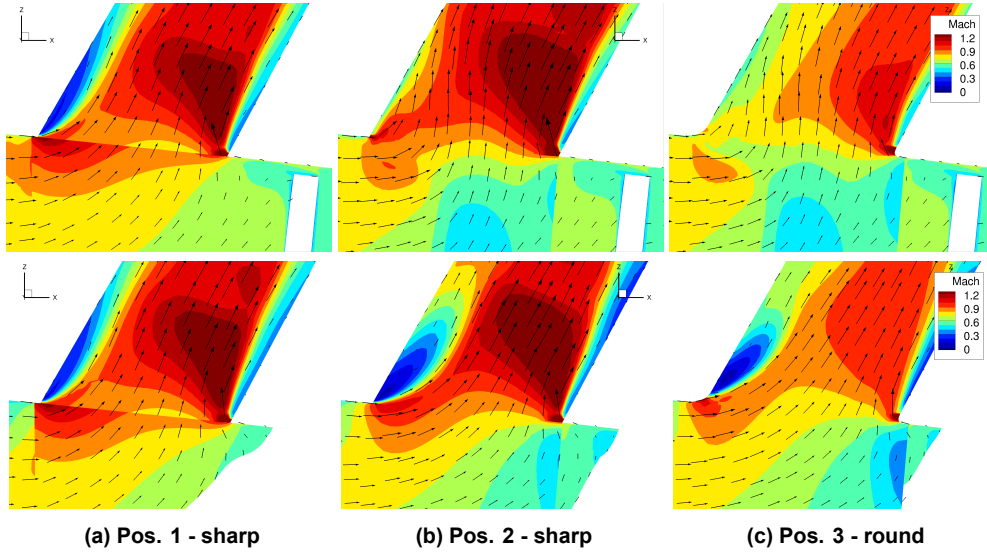


Figure 7 : Mach contour plots at EB01 bleed port on S2-planes at two different circumferential locations. Comparison of interface pos. 1 with sharp edges (a), pos. 2 with sharp edges (b) and pos. 3 with round edges (c) at bleed port EB01 with 20% extraction.

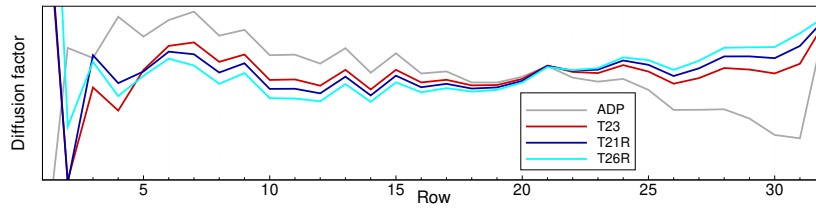


Figure 8 : Row-wise diffusion factor at MEL operation.

due to the high amounts of mass flow being extracted through EB01. This region is also visible in fig. 6. No significant difference in this back-flow region at the rotor tip can be observed for the three cases.

As for case 1 the mixing plane is positioned upstream of EB01, the wakes of stator 5 get mixed out before the extraction process occurs. This leads to an almost uniform inflow into the bleed port. On the contrary, for cases 2 and 3 the flow regime in the vicinity of the bleed port is highly non-axis-symmetric due to the wake of stator five. This also results in a non-axis-symmetric inflow into the bleed ports as can be observed in fig. 7, showing S2-slices at two different locations around the circumference. Especially the separation region inside the bleed port at the upstream edge shows significant differences between case 1 and the other two cases. Also visible in this plot is how the round corner of case 3 leads to smaller separation regions at the edges and an overall reduced Mach number inside the bleed port. Still, even with the sharp edges, the channel is not choking.

From these simulations, it can be concluded that a mixing plane position downstream of the bleed port leads to a more realistic flow into the bleed port. The backflow at the tip region is not affected by this interface position. Round edges lead to reduced separations and reduced Mach numbers inside the bleed port, but the general flow pattern is not significantly influenced by the sharp edges. Also, the possibility of locating the mixing plane slightly more upstream of the rotor blade is beneficial in terms of overall simulation stability, which can be associated with a lower interference of the rotor shock with the mixing plane in this case. Therefore, and as no significant differences between the three cases in terms of global performance data can be observed, case 2 is chosen for the following studies.

OPERATION AT MEL

At MEL, the compressor operates with a closed IGV and stator 1 at a reduced mass flow rate of about 55% compared to base-load. The closure of the IGV row unloads the first rotor/stage by reducing the flow incidence and decreasing its compression ratio to a value less than one. This leads to a loading shift towards the aft of the compressor as shown in fig. 8 in terms of diffusion factor (DF).

The flow conditions of the first stages at MEL are characterized by negative incidence, strong shocks, and separations. Fig. 9 shows Mach contours at relative channel heights of 25 and 75% for stages 1 to 3 for operation at MEL (T23). Visible is a negative incidence at rotor 1 with a separation at the pressure side which is especially high at the hub and mid section.

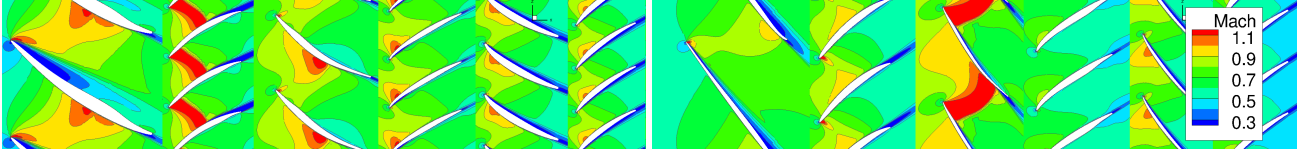


Figure 9 : Mach contours on S1-slices at relative channel heights of 25% and 75% for Stages 1,2 and 3) at MEL (T23).

| case | Δ Mass in [%] | ΔP tot out [%] | ΔT tot out [%] |
|------|----------------------|------------------------|------------------------|
| T23 | -0.01 | -0.13 | -2.00 |
| T21R | 2.12 | -0.07 | -1.14 |
| T26R | -1.10 | -1.19 | -1.28 |
| T28R | 0.30 | -0.11 | -1.33 |
| T30R | 1.73 | -0.18 | -1.54 |
| T32R | 0.23 | -1.26 | -1.85 |

Table 3 : Comparison of experimental and simulation data. Difference of simulation to experimental data.

Stator 1 shows a strong shock at these blade sections, with a shock-induced separation. At higher blade sections, rotor 2 has a strong passage shock. The following stators show blockage in the casing region.

COMPARISON WITH EXPERIMENTS

The experimental test cases listed in tab. 1 are simulated for validation purposes. T23 and T21R represent cases of compressor operation at MEL for different ambient conditions. T26R and T32R have a further closed IGV and reduced inlet mass flow rate. Cases T28R, T30R, and T32R, have an increased mass flow extraction through EB01 as compared to standard MEL operation.

As already stated, the boundary conditions at the inlet and exit are derived from measurement data. The mass flow extracted by the external bleeds has been calculated through a thermodynamic energy balance of the turbine exhaust diffuser. Heat balance calculations are done with a field-calibrated GT performance tool. The tool is a reliable method to calculate turbine efficiency and mass flow, which are not directly measurable.

Tab. 3 compares simulation results with experimental data in terms of relative error $\delta x = \frac{x_{SIM} - x_{EXP}}{x_{EXP}}$ of the experimental test cases. The accuracy of the simulations to predict the compressor inlet mass flow rate lies within a range of $\pm 2\%$. The total outlet temperature is slightly underestimated by 1-2% for all cases. Fig. 10 shows the total temperature and pressure distribution at the casing compared with the values measured by the temperature taps and pressure probes. The total temperature and pressure simulation results along the compressor match very well with the data for all experimentally tested operating conditions.

BLEED EXTRACTION STUDY

Using the setup described above, a matrix of different extraction rates for two different ambient temperature cases, 0°C (T0) and 15°C (T15) are simulated to analyze the compressor's performance and flow conditions under high extraction rates of mass flow through the first two bleed ports. Especially the stability limiting effects under such conditions are of interest.

Mass flow blow-off strongly impacts the cycle, as a part of the compressor air mass flow is compressed but does not participate in power generation. From a cycle efficiency standpoint, it is therefore beneficial to extract the air at the first bleed, at a lower pressure, and not at the following bleeds. Also, according to (Mosele et al., 2019), the further upstream the flow is extracted, the smaller the increase in DF at the last stage.

For both temperature cases, speed lines for four different extraction rates, as listed in tab. 4, are simulated. The back-pressure is increased with decreasing step sizes in order to obtain high accuracy in predicting the numerical stability limit.

A map of the simulations (fig. 11) shows how the pressure rise capability of the compressor drops for a decreasing outlet mass flow rate due to an increased blow-off through the bleed ports. An increase in ambient temperature leads to a drop in absolute pressure rise at WL conditions. However, the numerical stability margin in terms of relative pressure rise capability related to the WL appears to be higher as compared to a lower temperature.

For an increased blow-off, a decrease in efficiency can be observed, as for a reduced temperature. The additional losses can be attributed to the stages in the vicinity of the bleed ports in the case of an additional extraction, whereas in the case of a lower temperature, additional losses occur in the first stages and can be attributed to even higher incidences occurring at the MEL conditions.

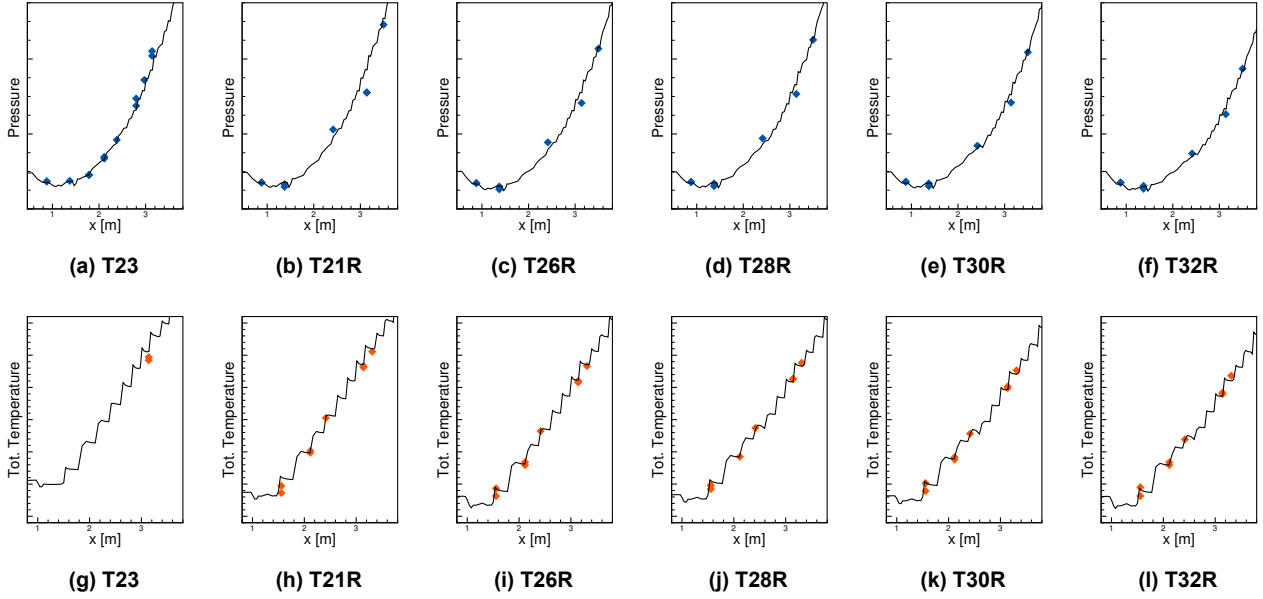


Figure 10 : Comparison of simulation results with experimental data.

| case | T_{amb} [K] | p_{amb} [hPa] | \dot{m}_{EB01} [% of \dot{m}_{in}] | \dot{m}_{EB02} [% of \dot{m}_{in}] | \dot{m}_{EB03} [% of \dot{m}_{in}] |
|-----------|------------------|--------------------|--|--|--|
| T00-00-00 | 273.15 | 1013 | MEL | MEL | MEL |
| T00-06-00 | 273.15 | 1013 | 06 | MEL | MEL |
| T00-12-00 | 273.15 | 1013 | 12 | MEL | MEL |
| T00-12-10 | 273.15 | 1013 | 12 | 10 | MEL |
| T15-00-00 | 288.15 | 1013 | MEL | MEL | MEL |
| T15-06-00 | 288.15 | 1013 | 06 | MEL | MEL |
| T15-12-00 | 288.15 | 1013 | 12 | MEL | MEL |
| T15-12-10 | 288.15 | 1013 | 12 | 10 | MEL |

Table 4 : Test matrix for the numerical blow-off study - MEL indicates conditions similar to standard MEL operation.

As expected, an increase in mass flow extraction leads to increased loading of the aft part of the compressor (fig. 12). Studies of the same engine by Ricci et al. (2021, 2022) with a different CFD solver and by Mosele et al. (2019) and Hedkvist (2019) with a through-flow solver, show similar trends regarding the change in loading due to a higher blow-off rate.

In terms of stage loading, an increase in the blow-off rate shows a similar tendency on the stage loading of the last stages as a drop of compressor inlet temperature does (fig. 12). Fig. 12a shows how the row-wise diffusion factor changes with increased bleed mass flow extraction relative to the nominal case. A significant drop, which depends on the rate of extraction, can be seen in the vicinity of the bleed ports. Towards the end of the compressor, however, an increase of DF is observed, which peaks at the last stator. The same tendency has already been reported in previous through-flow studies (Mosele et al., 2019; Hedkvist, 2019). The increase in diffusion factor of the last stages can similarly be observed when a drop in ambient temperature occurs, which is shown in fig. 12b, where the differences between cases T00 and T15 for the four blow-off rates are plotted.

The different change in stage-loading with an increased mass flow extraction through the bleeds leads to a change in the stage characteristics. Fig. 13 shows characteristics of stages 11 to 15, plotted between total pressure ratio and corrected mass flow rate \dot{m}_{corr} of the individual stage. The displayed range of total pressure ratio is the same for all stage plots. For nominal extraction at MEL stages 12, 13, and 15 all roll over, reaching their individual numerical stability limit almost simultaneously. For higher blow-off rates, the tendency of the stage characteristics to roll over decreases for stages 11 to 13 and increases for stage 15, resulting in stage 15 failing first. This is supported by the observation of a peaking increase in diffusion factor at the last stator.

Approximately identifying the compressor total pressure ratio at which either of the stage characteristics (fig. 13) peaks first, the numerical stability margin in terms of total-to-total pressure rise capability can be calculated. The pressure rise capability of the compressor normalized by the value at working line conditions $\Pi_{tt,n} = \Pi_{tt,SL}/\Pi_{tt,WL} - 1$ drops for case T15 from 16% at nominal blow-off to 15%, 13% and 8% for cases T15-06-00, T15-12-00 and T15-12-10, respectively (fig

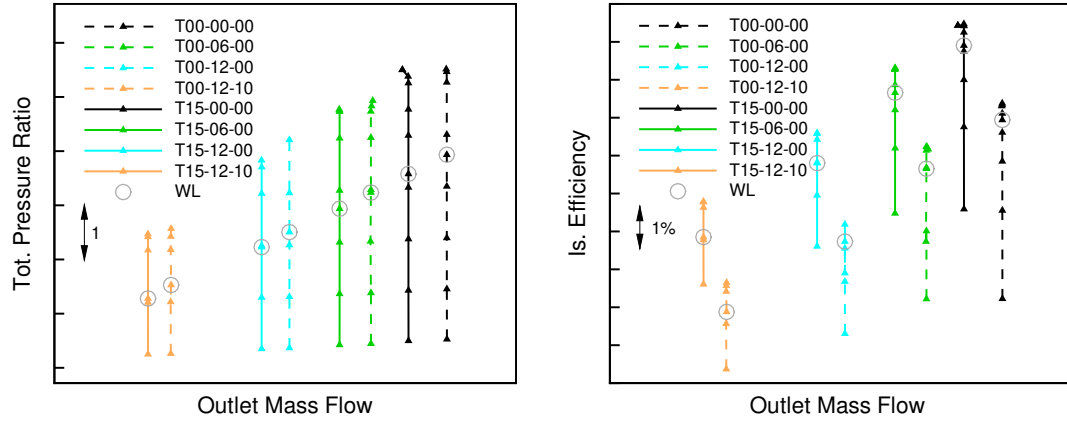
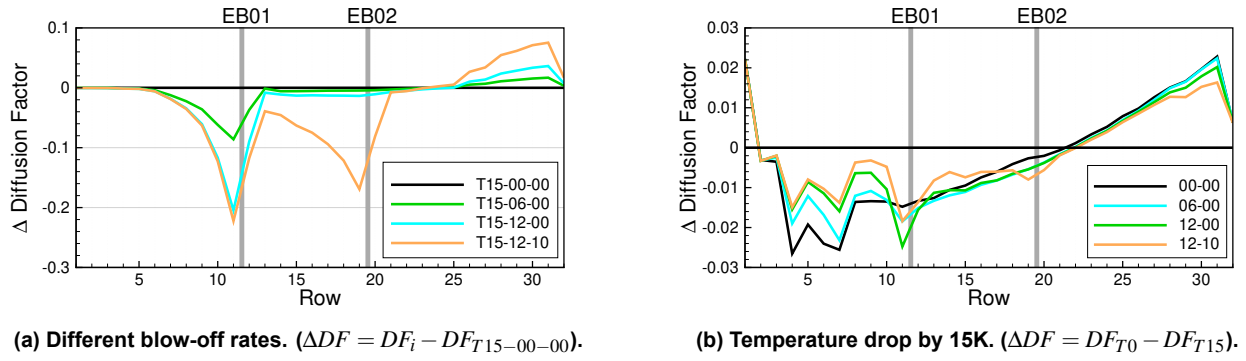


Figure 11 : Map of the test-matrix simulations.



(a) Different blow-off rates. ($\Delta DF = DF_i - DF_{T15-00-00}$).

(b) Temperature drop by 15K. ($\Delta DF = DF_{T0} - DF_{T15}$).

Figure 12 : Row-wise delta diffusion coefficient at WL conditions.

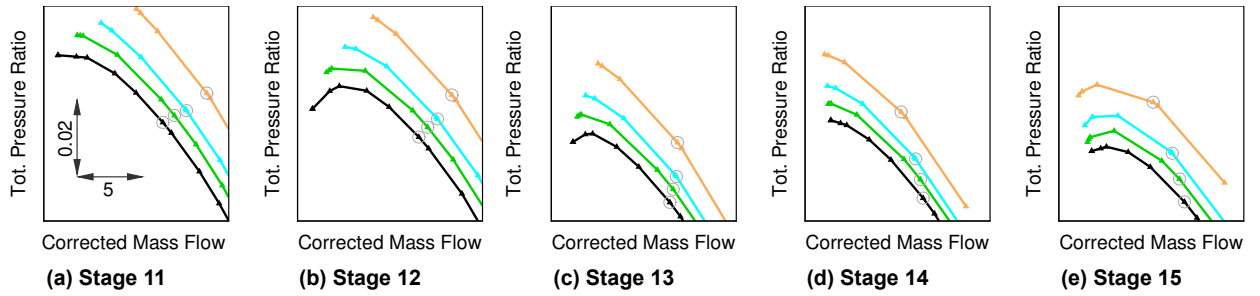


Figure 13 : Stage maps of T15 cases: T15-00-00, T15-06-00, T15-12-00 and T15-12-10.

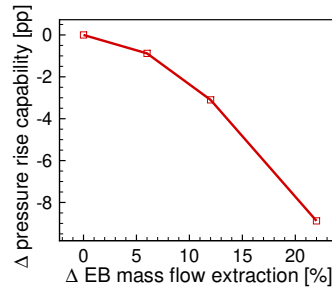
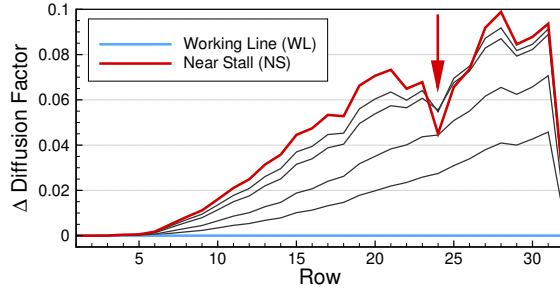
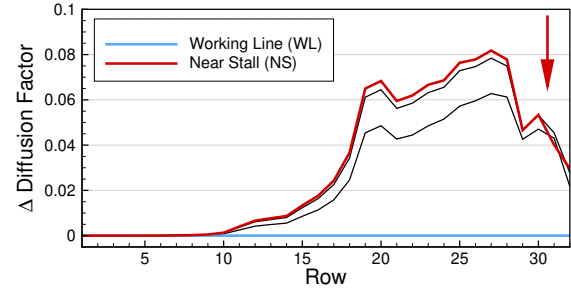


Figure 14 : Reduction in pressure rise capability for case T15 with increased blow-off rate.

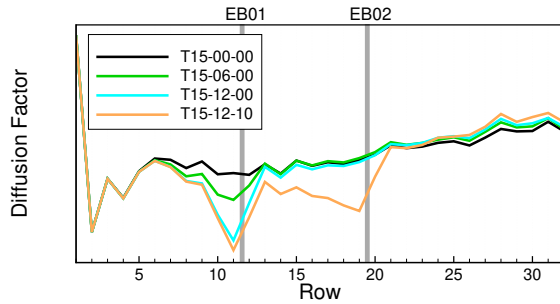


(a) Nominal EB extraction (T15-00-00)

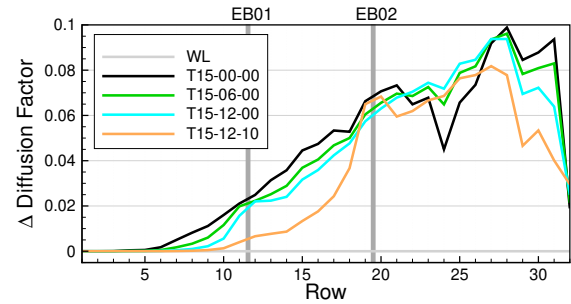


(b) Maximum EB extraction (T15-12-10)

Figure 15 : Change of row-wise diffusion factor relative to working line (WL) operation at MEL when throttling the compressor. Throttling levels correspond to the operating points of the speed lines in fig. 11.



(a) DF near numerical stability limit.



(b) Delta DF between WL and (near) numerical stability limit.

Figure 16 : Row-wise diffusion factor near numerical stability limit at MEL.

14), which has to be considered implementing this measure.

The increase in loading of the aft part of the compressor leads to a shift of the stage that appears to be triggering a flow breakdown at the numerical stability limit from stage 12 to stage 15. Fig. 15 shows the increase in row-wise diffusion coefficient when throttling the compressor at nominal blow-off extraction rates (fig. 15a) and maximum extraction rates (fig. 15b). For nominal extraction, the delta in diffusion factor continuously increases with higher amounts of throttling, especially at the rear stages, as expected. However, approaching the stability limit, the diffusion factor starts dropping at row 24, indicating that this row has reached its limit. At maximum extraction, on the contrary, rows 29 onward appear to reach their limit first, as the diffusion factor close to the numerical stability limit of the compressor is not increasing anymore for these rows and even drops at row 31, the last stator. With an increased blow-off, the last stages reach the highest absolute values of diffusion factor (fig. 16a), explaining why these stages fail first for maximum blow-off. Between the two cases of minimum and maximum extraction, the increase in loading at near stall conditions changes gradually (fig. 16).

A closer flow field investigation confirms how the stability-limiting effect changes with an increased blow-off. For nominal extraction, a blockage area developing in the rotor 12 tip area (figs. 17a and 17b), as well as in the neighboring rotors, leads to a flow breakdown. For maximum extraction, the rotor tip blockage areas of stages 11 to 14 are also visible close to the numerical stability limit (second to last OP), but to a reduced extent. Instead, in this case, a dominant blockage area in the last stage develops.

LIMITATIONS OF THE CFD MODEL

To further assess the credibility of the numerical results, several simulations are repeated with mesh 3. Comparing simulation results obtained with meshes 2 and 3, a difference in the prediction of the secondary flow structure starts to appear close to the numerical stability limit. At maximum blow-off, this leads to a slightly different prediction of the stability limiting mechanism. Whereas with mesh 2 the limiting blockage occurs at the casing, with mesh 3, a hub corner separation in the last stages develops (figs. 17c and 17d). This corner separation leads to a flow redistribution to the higher blade sections accelerating the flow close to the casing and reducing the developing blockage areas near the casing. At lower extraction rates, differences in the magnitude of the low momentum areas close to the end-walls become visible but with no influence on the stability limiting mechanism. At working line conditions, no differences in terms of flow structures between the two meshes are observed. The numerical stability limit is not changed significantly, with a tendency for mesh 3 to fail at a slightly higher back-pressure.

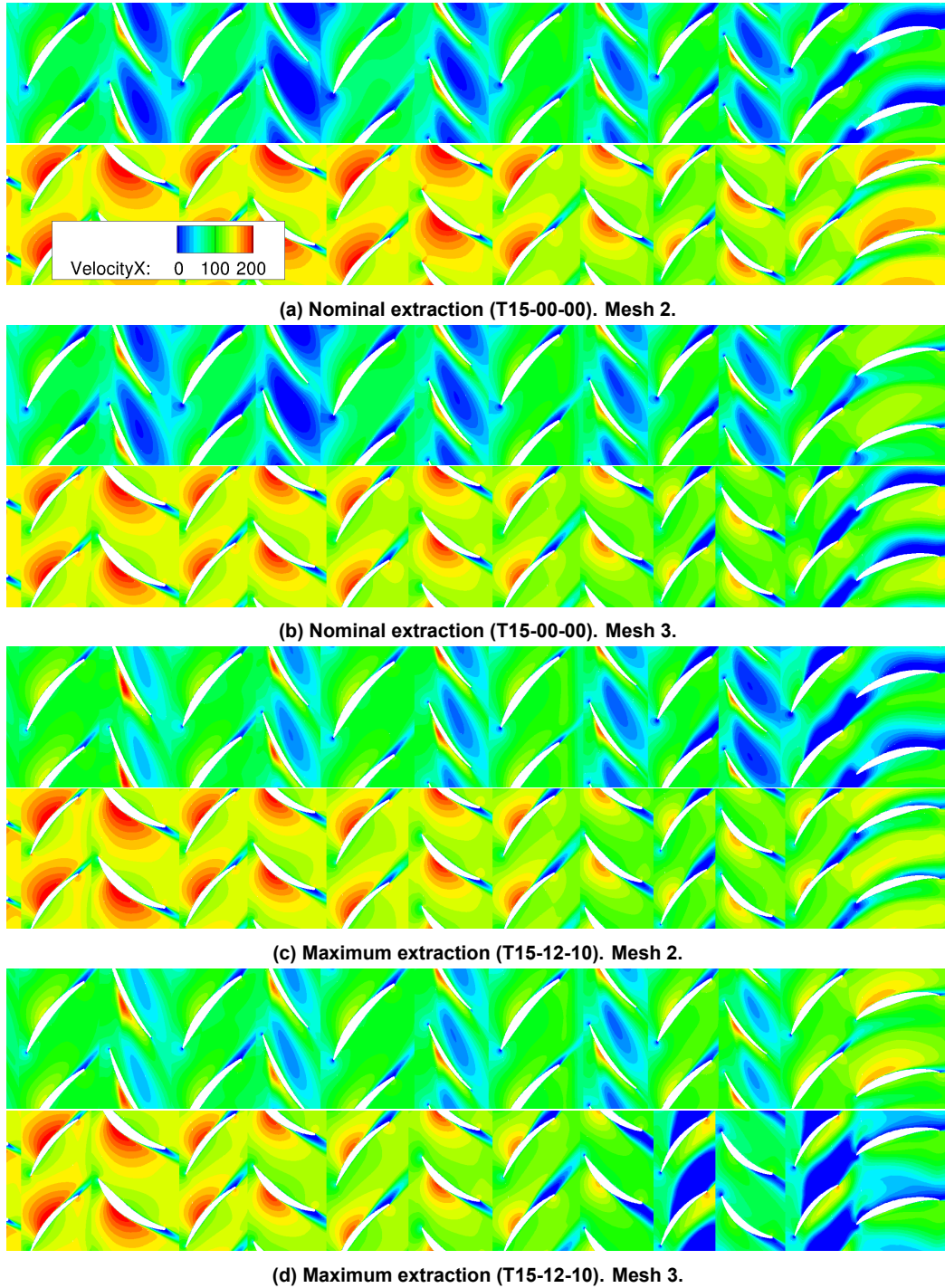


Figure 17 : Regions of separation and blockage in the rear stages (stator 10 to OGV) visualized by means of axial velocity for nominal blow-off and maximum blow-off at the numerical stability limit. $h_{rel} = 95\%$ (top), $h_{rel} = 5\%$ (bottom).

Although these effects do not have any influence on the general outcome of this study, it is worth noting that even though two meshes show good agreement at working line conditions in a simulation of a multistage axial compressor, differences can start to appear close to the numerical stability limit, which was also observed by Cornelius et al. (2013).

It is known that further influencing factors on the numerical stalling behavior are the turbulence model (Cornelius et al., 2013) and the cavity flows. The influence of the turbulence model is not analyzed in this study. Also, cavity flows have not been considered in the numerical setup, which would lead to changes in the end-wall flow structure and radial mixing (Wang et al., 2018; Cozzi et al., 2017, 2018).

Overall, it has to be recognized that at extreme off-design conditions, close to the stability limit, the accuracy of a steady-state RANS simulation will decrease and there is increasing uncertainty, especially regarding the details of the flow field in a multistage machine. The general outcome of this study, however, remains unaffected. At MEL working line conditions, experiments and numerical results agree very well, even for high blow-off rates. Therefore, it can be assumed that the trend regarding the change in loading caused by increased blow-off rates is predicted accurately.

CONCLUSION

An extensive study of the flow in an Ansaldo Energia heavy-duty F-Class gas turbine compressor at MEL conditions with increased blow-off rates through the bleeds has been performed by means of full compressor 3D CFD simulations. The simulations show good agreement with experimental data from a test campaign at an Ansaldo Energia power plant, confirming that CFD can accurately predict the flow at MEL conditions.

Effects on performance and operability of a blow-off valve opening, with the aim of reducing the Minimum Environmental Load and increasing the compressor flexibility, have been studied. A parametric study with different blow-off rates from the first two external bleeds and at two ambient temperatures has been performed to analyze the effect of an increased blow-off rate as a means for MEL reduction. Up to 12% of air extraction from core stages and additionally 10% of air extraction from rear stages have been investigated by CFD. The simulations demonstrate that a significant blow-off rate is possible while maintaining a stable operation of the compressor.

As expected, the additional blow-off increases the loading of the rear part of the compressor and especially in the last stage. This leads to a progressive reduction of the stability margin with increasing blow-off rates, limiting the maximum possible air extraction through the bleed ports. The quantification of these effects for an operation at MEL and, in particular, the quantification of the impact of bleed extraction rates on the stability at MEL confirms the viability of the approach as a turndown strategy. Also, it is confirmed that extraction at the first bleed is possible and should be preferred, as it is favorable in terms of performance and stability. Further analyses should verify the integrity of the whole GT at operation under conditions with increased blow-off rates.

In conclusion, the presented study confirms that blow-off air extraction is a suitable measure to enable a more flexible operation of gas turbines, both for new units and as a retrofittable technological feature for existing engines. The extended low part-load capability will allow the operation of a power plant in a single and combined cycle mode with high efficiency and rapid changes in load as demanded by the grid.

ACKNOWLEDGMENTS

These research results are part of the TURBO-REFLEX project, which has received funding from the European Union's Horizon 2020 research and innovation program under grant agreement No 764545.

NOMENCLATURE

Abbreviations

| | |
|-------|-----------------------------|
| ADP | Aerodynamic Design Point |
| B | (Rotor) Blade |
| BO | blow-off |
| CCGTs | Combined cycle gas turbines |
| CO | Carbon monoxides |
| DF | Diffusion Factor |
| EB | External bleed |
| IGV | Inlet guide vane |
| MEL | Minimum environmental load |
| NOx | Mono-nitrogen oxides |
| NS | Near stall |
| OP | Operating point |
| pp | percent points |
| RH | Relative Humidity |
| SAS | Secondary air system |
| SL | Stability limit |
| V | Vane |
| VIGV | Variable Inlet Guide Vane |
| WL | Working line |

Subscripts

| | |
|------|----------------|
| amb | ambient |
| corr | corrected |
| n | normalized |
| rel | relative |
| tot | total |
| tt | total to total |

Symbols

| | |
|-----------|------------------|
| h | (channel) height |
| \dot{m} | Mass flow |
| Ma | Mach number |
| p | Pressure |
| T | Temperature |

Greek Symbols

| | |
|----------|----------------|
| γ | Stagger angle |
| Δ | Delta |
| Π | Pressure ratio |

REFERENCES

- Becker, K., Heitkamp, K. and Kügeler, E. (2010), ‘Recent progress in a hybrid-grid CFD solver for turbomachinery flows’, *fluid dynamics ECCOMAS CFD*.
- Cioffi, M., Piola, S., Puppo, E., Silingardi, A. and Bonzani, F. (2014), Minimum environmental load reduction in heavy duty gas turbine by bleeding lines, in ‘ASME Turbo Expo 2014: Turbine Technical Conference and Exposition’, American Society of Mechanical Engineers Digital Collection, pp. V03AT09A002–V03AT09A002.
- Cornelius, C., Biesinger, T., Galpin, P. and Braune, A. (2013), Experimental and computational analysis of a multistage axial compressor including stall prediction by steady and transient CFD methods, in ‘ASME Turbo Expo 2013: Turbine Technical Conference and Exposition GT2013’, pp. 1–12.
- Cozzi, L., Rubecchini, F., Giovannini, M., Marconcini, M., Arnone, A., Schneider, A. and Astrua, P. (2018), Capturing radial mixing in axial compressors with CFD, in ‘ASME Turbo Expo 2018: Turbomachinery Technical Conference and Exposition’, American Society of Mechanical Engineers, pp. V02CT42A025–V02CT42A025.
- Cozzi, L., Rubecchini, F., Marconcini, M., Arnone, A., Astrua, P., Schneider, A. and Silingardi, A. (2017), Facing the challenges in CFD modelling of multistage axial compressors, in ‘ASME Turbo Expo 2017: Turbomachinery Technical Conference and Exposition’, American Society of Mechanical Engineers Digital Collection.
- Eulitz, F. (1999), A RANS method for the Time-Accurate simulation of Wake-Induced Boundary-Layer transition in turbine flows, in ‘Papers from the Fourteenth International Symposium on Air Breathing Engines’, number ISABE99-7275, American Institute of Aeronautics and Astronautics.
- Giles, M. (1990), Non-reflecting boundary conditions for the euler equations, Technical report, MIT CFD Lab.
- Gonzalez-Salazar, M. A., Kirsten, T. and Prchlik, L. (2018), ‘Review of the operational flexibility and emissions of gas- and coal-fired power plants in a future with growing renewables’, *Renewable Sustainable Energy Rev.* **82**, 1497–1513.
- Hedkvist, S. (2019), Throughflow study on bleeding for part load compressor operation, Master’s thesis, Luleå University of Technology.
- Holmes, D. G. (2008), ‘Mixing planes revisited: A steady mixing plane approach designed to combine high levels of conservation and robustness’, *ASME Conference Proceedings* **2008**(43161), 2649–2658.
- Hummel, F. (2002), ‘Wake–Wake interaction and its potential for clocking in a transonic High-Pressure turbine’, *J. Turbomach.* **124**, 69–76.

- Hung, W. S. Y. (1993), 'Carbon monoxide emissions from gas turbines as influenced by ambient temperature and turbine load', *J. Eng. Gas Turbine. Power* **115**(3), 588–593.
- Lorenczik, S., Kim, S., Wanner, B., Bermudez Menendez, J. M., Remme, U., Hasegawa, T., Keppler, J. H., Mir, L., Sousa, G., Berthelemy, M. and others (2020), Projected costs of generating electricity-2020 edition, Technical report, Organisation for Economic Co-Operation and Development.
- Magni, F., Grimm, F., Sorato, S. and Micheli, M. (2016), GT13E2 low part load operation: Extended flexibility down to 30% load, in 'ASME Turbo Expo 2016: Turbomachinery Technical Conference and Exposition', American Society of Mechanical Engineers, pp. V003T08A008–V003T08A008.
- Malavasi, F., Pesce, P., Pesenti, A. V., Traverso, P. and Zito, D. (2013), Ansaldo AE94.3A combustion improvement towards flexibility through extensive field testing, in 'ASME Turbo Expo 2013: Turbine Technical Conference and Exposition', American Society of Mechanical Engineers Digital Collection.
- Mosele, S. G., Garbarino, T., Schneider, A., Cozzi, L., Arnone, A., Goinis, G. and Hedkvist, S. (2019), 'Compressor retrofittable solutions in Heavy-Duty gas turbines for minimum environmental load reduction', *E3S Web of Conferences* **113**, 01012.
- Nag, P., Little, D., Plant, A. and Roth, D. (2010), Low load operational flexibility for siemens F- and G-Class gas turbines, in 'ASME Turbo Expo 2010: Power for Land, Sea, and Air', American Society of Mechanical Engineers Digital Collection, pp. 15–21.
- Nag, P., Little, D., Teehan, D., Wetzl, K. and Elwoo, D. (2008), Low load operational flexibility for siemens g-class gas turbines.
- Ricci, M., Benvenuto, M., Mosele, S. G., Pacciani, R. and Marconcini, M. (2021), 'Impact of compressor flexibility improvements on heavy-duty gas turbine for minimum and base load conditions', *SSRN Electron. J.* .
- Ricci, M., Mosele, S. G., Benvenuto, M., Astrua, P., Pacciani, R. and Marconcini, M. (2022), 'Retrofittable solutions capability for gas turbine compressors', *International Journal of Turbomachinery, Propulsion and Power* **7**(1), 3.
- Roe, P. L. (1981), 'Approximate riemann solvers, parameter vectors, and difference schemes', *J. Comput. Phys.* **43**(2), 357–372.
- Saxer, A. P. and Giles, M. B. (1993), 'Quasi-three-dimensional nonreflecting boundary conditions for euler equations calculations', *J. Propul. Power* **9**(2), 263–271.
- Schmitt, S., Eulitz, F., Wallscheid, L., Arnone, A. and Marconcini, M. (2001), Evaluation of unsteady CFD methods by their application to a transonic propfan stage, in 'ASME Turbo Expo', New Orleans, Louisiana, USA.
- Therkorn, D., Gassner, M., Lonneux, V., Zhang, M. and Bernero, S. (2015), CCPP operational flexibility extension below 30% load using reheat burner Switch-Off concept, in 'ASME Turbo Expo 2015: Turbine Technical Conference and Exposition', American Society of Mechanical Engineers, pp. V003T20A007–V003T20A007.
- van Leer, B. (1979), 'Towards the ultimate conservative difference scheme v: a second order sequel to godunov' method', *J. Comput. Phys.* **32**(May 2016), 101–136.
- Wang, F., Carnevale, M., di Mare, L. and Gallimore, S. (2018), 'Simulation of multistage compressor at Off-Design conditions', *J. Turbomach.* **140**(2), 021011.
- Yang, H. and Weber, A. (2002), A conservative zonal approach with applications to unsteady turbomachinery flows, in 'Deutscher Luft- und Raumfahrtkongress', Stuttgart, Germany.